IEEE Access
Multidisciplinary | Rapid Review | Open Access Journal

Received 3 October 2023, accepted 17 October 2023, date of publication 20 October 2023, date of current version 26 October 2023.

Digital Object Identifier 10.1109/ACCESS.2023.3326372

RESEARCH ARTICLE

Mechanism Development and Pulse-Width Modulation Advanced Controller Design of Low Torque Manipulator

JIM-WEI WU[1], (Member, IEEE), TZU-LIN LEE[1], YOU-CHENG YAN[1], CHUAN-AN CHOU[1], AND CHENG-CHANG HO[2]

[1]Department of Electrical Engineering, National Central University, Taoyuan City 320317, Taiwan
[2]Department of Electronic Engineering, Lunghwa University of Science and Technology, Taoyuan City 333326, Taiwan

Corresponding author: Cheng-Chang Ho (james.ho701010@gmail.com)

This work was supported by the National Science and Technology Council of Taiwan under Grant MOST 111-2221-E-008-099 and Grant NSTC 112-2221-E-008-095.

ABSTRACT In most conventional robotic arms, the motors are installed on the rotating shafts within the arm, which means that the shape and size of the motors must be considered in the design of the arm, while the weight of the motors increases the torque on the supporting joints generated during arm movements. This paper presents a dual-axis robotic arm with the motors installed on the base of the device to overcome these issues. Movement around the first axis is driven by a gear, while that of the second axis is driven by a belt. Trajectory tracking is controlled by an adaptive sliding mode controller (ASMC). In simulations and experiments, the proposed robotic arm outperformed arms using PID control and sliding mode control (SMC) in terms of tracking accuracy and stability.

INDEX TERMS Robotic arm, low torque, adaptive sliding mode control, tracking error.

I. INTRODUCTION

Robotic arms are widely used to improve manufacturing efficiency and product quality, while reducing labor costs and improving safety [1], [2]. Manipulator accuracy, load capacity, stability, and response speed vary with the intended function of the arm.

The stability of robotic arms depends on the size and structural design of the arm as well as the control system. Roy and Whitcomb [3] compared the structural benefits of various linkage designs for robot arms with 2 degrees of freedom (2)-DOF) and a semi-direct drive system, including the parallelogram linkage, double parallelogram linkage, double-kite linkage, and band-drive. Yadmellat et al. [4] applied magnetorheological (MR) clutches to the same class of robotic arms to reduce joint impedance and ensure smooth motions. Kim et al. [5] developed a novel balance mechanism for a 6-DOF robotic arm, which uses a spring and slider crank within a double-parallelogram mechanism based on bevel gear units. Min et al. [6] developed a passive counterbalance mechanism (CBM) based on springs and wires to compensate for gravitational effects arising from the roll and pitch joint motions of a wall-mounted robotic arm. Huang et al. [7] developed a robotic arm with a spherical joint module, a rotary joint module, and a hybrid serial-parallel electric drive system. Groenhuis et al. [8] developed a multi-axis stepping motor capable of multiple DOF actuation to enable the coaxial driving of three arm joints. Korayem et al. [9] used robotic chains to form a closed-loop for application in cooperative robots, which can break through the limitations of frictional contact between the end effector and object. Aghajari et al. [10] proposed a new structure of robotic chain that gear can generate linear motion; this structure has a simple mechanism and provides an extended workspace for robotic equipment.

Numerous control methods have been developed to enable reliable high-accuracy trajectory tracking. Baek et al. [11] combined adaptive time-delay control (ATDC) with sliding mode control (SMC) to track the trajectory of a robotic arm. Note that ATDC uses delayed signals to eliminate nonlinear

The associate editor coordinating the review of this manuscript and approving it for publication was Mohammad Alshabi.

dynamics and interference terms, while adjusting the control gain adaptively to suppress chattering. Guo et al. [12] proposed an adaptive neural network control (ANNC) with backstepping to train an unknown model in the real-time adjustment of parameter weights according to system state errors. Zhu et al. [13] proposed a controller to preserve high-precision trajectory tracking and transient response times under the effects of neutral uncertainty and dead zone nonlinearity. Nubert et al. [14] proposed a model predictive control (MPC) function that uses a neural network to reduce computation time with discrete planning and control layers to reduce the complexity of tracking control tasks. Xiao et al. [15] proposed an adaptive fault-tolerant control method that simultaneously considers actuator faults, disturbances, and uncertainty in joint velocity measurements. Lee et al. [16] proposed dynamic adaptive gain for use in time delay control (TDC) systems to overcome the fact that constant (i.e., non-adaptive) gain cannot ensure accurate trajectory tracking under changing loads. Lin et al. [17] developed a dual-loop strategy to ensure robust model control in dynamic trajectory adaptation. Their control methodology is partitioned into external and internal loop controls. The external loop control employs recursive least squares estimation to plan the trajectory dynamically, while the internal loop control employs model-reaching control to linkage the trajectory and the tracking error.

In the current study, we proposed a new 2-DOF robotic arm mechanism to improve the torque and weight issues of conventional robotic arms, in which the motors are installed on the base to reduce the unwanted torque induced and potentially increase the stability during robotic arm movement. Movement around the first axis is driven by a gear, while that of the second axis is driven by a belt. The links, shafts, and motor seats were all designed to ensure easy assembly. We also developed an adaptive sliding mode controller (ASMC) for trajectory tracking to overcome disturbances and modeling uncertainty, while reducing dependence on artificially sliding surface parameter adjustments.

The remainder of this paper is organized as follows. Section II outlines the design of the manipulator hardware. Section III describes the proposed ASMC control system. Section IV presents simulation results for three trajectory tracking control schemes. Section V presents the results of experiments aimed at assessing the tracking performance of the proposed scheme. Conclusions are drawn in Section V.

II. MANIPULATOR HARDWARE DESIGN

This study sought to resolve the problems of conventional robotic arms in which the motor is installed on the rotating shaft, which increases the weight of the arm and the corresponding torque generated by arm movements. We also sought to facilitate assembly and disassembly of the arm for repairs.

A. HARDWARE DESIGN: MANIPULAR

Fig. 1 illustrates the configuration of the proposed robotic arm. Table 1 lists the specifications of the components.

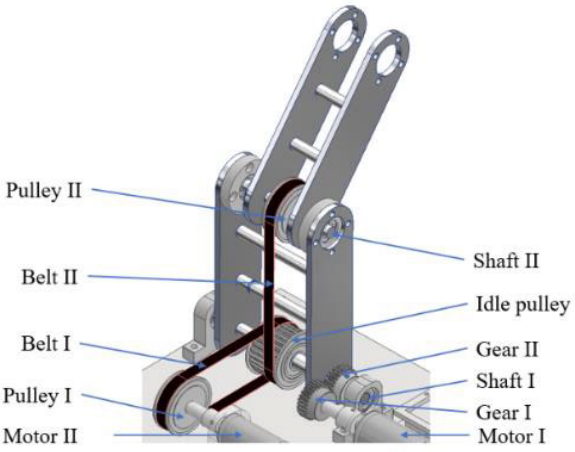

FIGURE 1. Mechanical structure of proposed robotic arm.

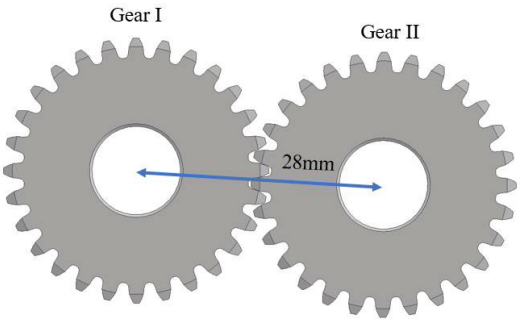

FIGURE 2. Gear mesh diagram of 28 mm datum circle diameter.

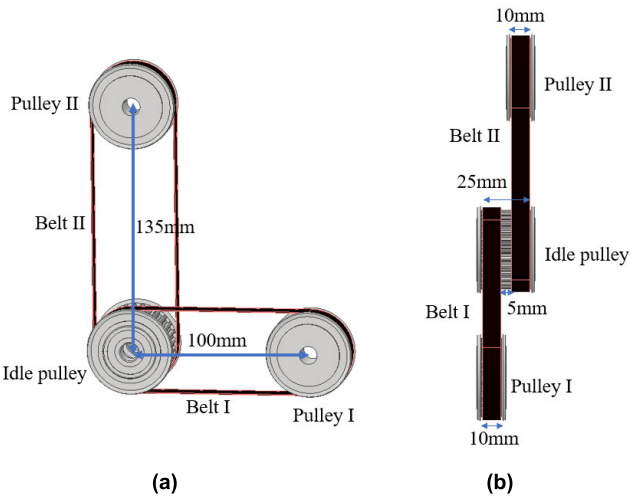

FIGURE 3. Assembly diagram of pulleys and belts: (a) Front view; (b) Side view.

Among them, the specifications of Gear I and Gear II are the same because they are only used for transmission, and since their datum circle diameter is 28 mm, the distance between the centers of the two gears for complete engagement is 28 mm, as shown in Fig. 2. Pulley I, Pulley II, and Idler pulley's pitch circle diameters are all 44.56 mm and are only used for transmission. Pulley I and Pulley II have the same specifications and are suitable for using a belt width of

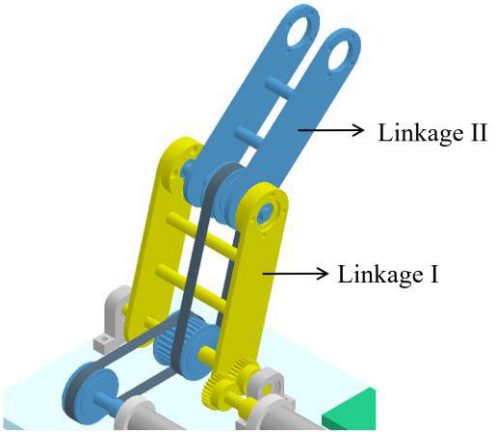

FIGURE 4. Schematic illustration showing the 2-DOF robotic arm.

TABLE 1. Specifications of mechanical components.

Part Name	Specification	
Gear I	Datum circle diameter: 28 mm	28 teeth
Gear II	Datum circle diameter: 28 mm	28 teeth
Pulley I	pitch circle diameter：44.56 mm	Suitable belt width: 10 mm
Pulley II	pitch circle diameter：44.56 mm	Suitable belt width: 10 mm
Idle pulley	pitch circle diameter：44.56 mm	Suitable belt width: 25 mm
Belt I	length: 340 mm	width: 10 mm
Belt II	length: 410 mm	width: 10 mm

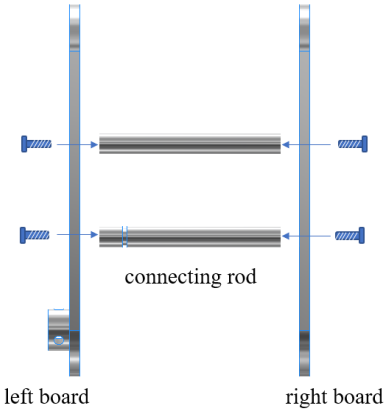

FIGURE 5. Linkage assembly.

10 mm. The idle pulley is a transmission part between the two pulleys and requires at least 20 mm of space to accommodate two 10 mm belt widths. Therefore, we chose an Idle pulley with a belt width of 25 mm to reserve a gap of 5 mm between the two belts. Fig. 3(a) and (b) show the assembly diagram of the pulleys and belts, which detail the components' size and

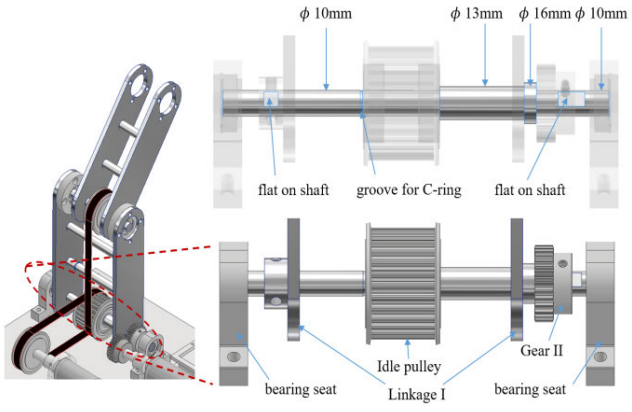

FIGURE 6. Assembly of Shaft-I.

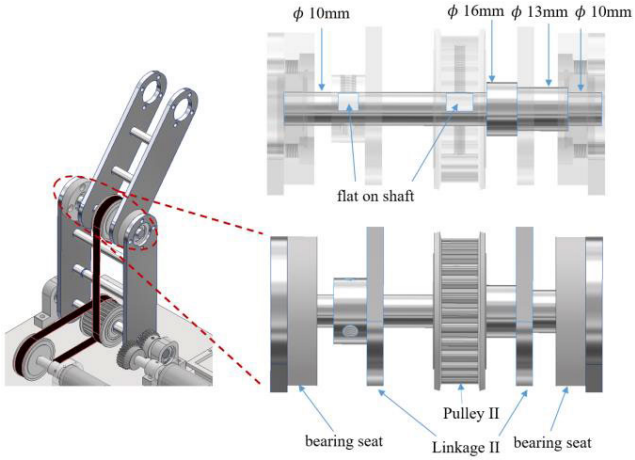

FIGURE 7. Assembly of Shaft-II.

relative position in front and side views. As shown in Fig. 4, Linkage-I (yellow) alters the position of Linkage-II (blue).

B. LINKAGE DESIGN

We adopted a hollow linkage design to minimize the weight of the robot arm. As shown in Fig. 5, the two beams in the linkages are locked together by screws passing through the beams into connecting rods. The protruding cylinder at the lower end of the left beam has three screw holes evenly spaced around the circumference (i.e., at angles of 120 degrees), which is used to secure the linkage assembly on the shaft. There are large holes at the top of the beams providing a seat for circular bearings surrounded by four holes for mounting screws. Note that the left and right beams used in Linkage-I are identical to those in Linkage-II. The only difference between the two linkages is the length of the respective connecting rods.

C. SHAFT DESIGN

The design of the shaft was meant to facilitate the stable attachment of various mechanical components. As shown in Figs. 6 and 7, the diameter of the shafts and holes through the components on the left side (Gear-I, idler pulley, bearing

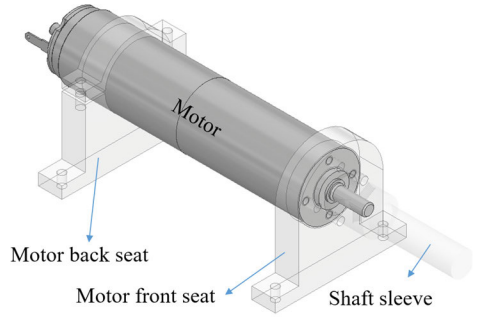

FIGURE 8. Schematic diagram of motor seat and shaft sleeve.

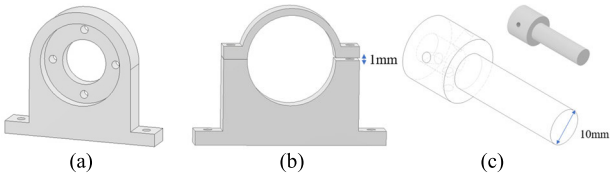

FIGURE 9. (a) Motor front seat; (b) Motor back seat; (c) Shaft sleeve.

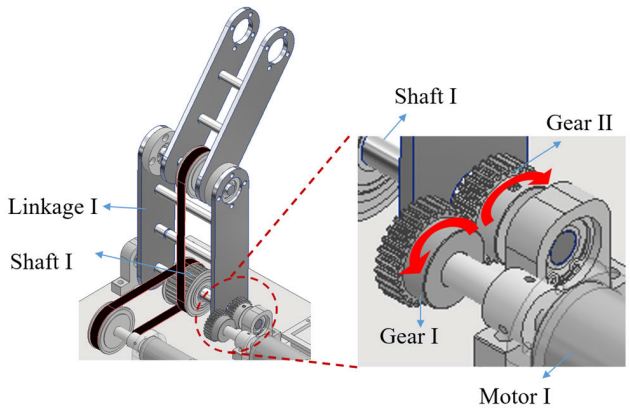

FIGURE 10. Gear-drive system for Linkage-I.

housing) are all 10 mm, while the diameter of the shafts on the right side varies step-wise between 16 mm, 13 mm, and 10 mm to enable the clamping of various components securely in place with minimal locking devices. Note that the idle pulley is held in place between the 13 mm section of the shaft on one side and a C-ring set within a groove on the other side. Flat sections were also cut into the shaft to enhance the stability of locking screws.

D. MOTOR SEAT AND SHAFT SLEEVE

As shown in Fig. 8, the motor assembly includes front and back motor seats to minimize vibration and a shaft sleeve to connect the gear assembly. The front seat provides a groove into which the motor is inserted with four screw holes corresponding to holes on the motor (Fig. 9(a)) and the upper section of the back seat can be adjusted vertically by screws to lock the motor securely in place (Fig. 9(b)). A sleave is fit over the motor shaft to increase the diameter to 10 mm, which corresponds to the diameter of the hole in the gear assembly

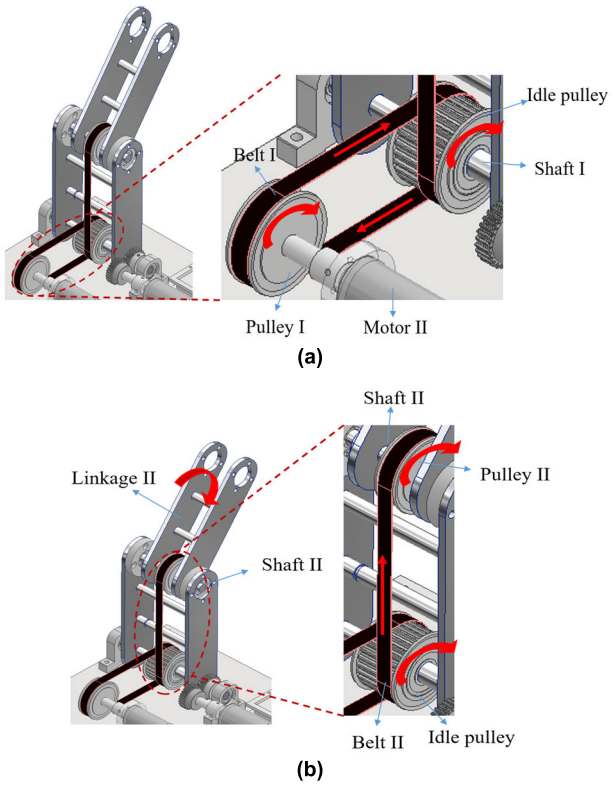

FIGURE 11. Belt-drive system for Linkage-II: (a) Belt I; (b) Belt II.

(Fig. 9(c)). Note that the sleeve is tightly locked to the front end of the motor via three screw holes evenly spaced around the circumference (i.e., at angles of 120 degrees).

E. GEAR DRIVE

Fig. 10 illustrates the configuration of the gears driving Linkage-I, where Gear-I and Gear-II have the same number of teeth and Linkage-I and Gear-II are attached to the same shaft (Shaft-II). Thus, any counterclockwise rotation of Motor-1 and Gear-I causes an equal clockwise rotation of Gear-II as well as Linkage-I.

F. BELT DRIVE DESIGN

Fig. 11 shows the belt-drive system used for Linkage-II. As shown in Fig. 11(a), Motor-II is connected to Pulley-I, such that any clockwise rotation of Motor-II and Pulley-I causes an equal clockwise rotation of Belt-I and the Idle pulley. As shown in Fig. 11(b), the rotation of the Idle pulley causes a corresponding clock-wise rotations of Belt-II, Pulley-II and also Linkage-II to which Pulley-II is attached. Note that a bearing between the Idle pulley and Shaft-I ensures that the rotation of the Idle pulley does not affect Linkage I.

III. MODELING AND CONTROLLER DESIGN

The relationship between angular velocity ω_m and the input voltage u_v of the DC motor in Fig. 12 can be expressed in accordance with the electrical and mechanical equations

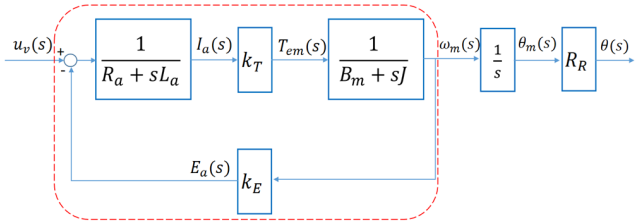

FIGURE 12. Transfer function of motor.

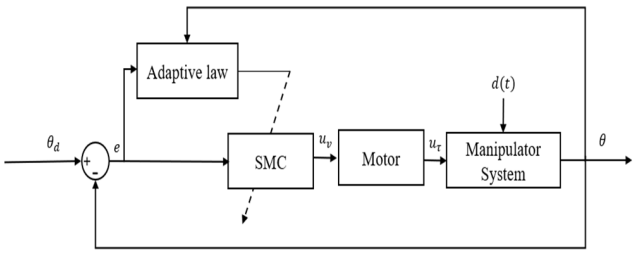

FIGURE 13. Schematic diagram of proposed controller.

in [18] as follows:

$$G(s) = \frac{\omega_m(s)}{u_v(s)} = \frac{k_T/R_a}{(B_m + sJ) + k_E k_T/R_a} \tag{1}$$

where k_E is the back-EMF constant of the motor measured using $\frac{V}{\frac{rad}{s}}$, k_T is the torque constant of the motor measured using Nm/A, while R_a is the terminal resistance of the motor measured in terms of Ω, J is the rotor inertia of the motor measured in terms of kgm^2, and B_m is the viscous friction constant of the motor, the unit of which is Nms/rad. However, B_m cannot be obtained from motor specifications, but it can be calculated by the following:

$$B_m = \frac{k_T \times I_{nl}}{V_{nl}} \tag{2}$$

where I_{nl} is the no-load current, V_{nl} is the no-load speed, and k_T is the motor torque constant. According to the Eq. (1), the angle of the motor θ_m can be expressed as:

$$\theta_m(s) = \frac{k_T/R_a}{s[(Js + B_m) + \frac{k_E k_T}{R_a}]} u_v(s) \tag{3}$$

Using inverse Laplace transformation on Eq. (3):

$$J\ddot{\theta}_m + \left(B_m + \frac{k_E k_T}{R_a}\right)\dot{\theta}_m = \frac{k_T}{R_a} u_v \tag{4}$$

The above equations are all considering the case of no-load on the motor. In order to evaluate the situation of installing a mechanical arm, Eq. (4) can be expressed as:

$$J\ddot{\theta}_m + \left(B_m + \frac{k_E k_T}{R_a}\right)\dot{\theta}_m = \frac{k_T}{R_a} u_v - \frac{u_\tau}{R_R} \tag{5}$$

where u_τ represents the control torque vector, and R_R is the reduction ratio of each motor. We define the joint angle of the robot arm as θ, which can get $\theta_m = R_R \times \theta$, and we can rewrite Eq. (5) as:

$$R_R^2\left[J\ddot{\theta} + \left(B_m + \frac{k_E k_T}{R_a}\right)\dot{\theta}\right] = R_R \frac{k_T}{R_a} u_v - u_\tau \tag{6}$$

We use the Lagrangian formulation [19], [20] to establish the dynamic model of the proposed manipulator:

$$u_\tau = M(\theta)\ddot{\theta} + C\left(\theta, \dot{\theta}\right) + G(\theta) \tag{7}$$

$$M(\theta) = \sum_{i=1}^{2}\left(J_{vi}^T m_i J_{vi} + J_{\omega i}^T I_i J_{\omega i}\right) \tag{8}$$

$$C\left(\theta, \dot{\theta}\right) = \begin{bmatrix} \sum_{j=1}^{2}\sum_{k=1}^{2}\left(\frac{\partial M_{1j}}{\partial \theta_k} - \frac{1}{2}\frac{\partial M_{1k}}{\partial \theta_1}\right)\dot{\theta}_j\dot{\theta}_k \\ \sum_{j=1}^{2}\sum_{k=1}^{2}\left(\frac{\partial M_{2j}}{\partial \theta_k} - \frac{1}{2}\frac{\partial M_{2k}}{\partial \theta_2}\right)\dot{\theta}_j\dot{\theta}_k \end{bmatrix} \tag{9}$$

$$G(\theta) = \begin{bmatrix} \sum_{i=1}^{2}\left(m_i g^T J_{vi}^1\right) \\ \sum_{i=1}^{2}\left(m_i g^T J_{vi}^2\right) \end{bmatrix} \tag{10}$$

where $M(\theta)$ is the inertia matrix, $C\left(\theta, \dot{\theta}\right)$ is the centripetal and coriolis force vector, and $G(\theta)$ is the gravitational force vector, while J_{vi} and $J_{\omega i}$ are the Jacobian matrices of linear velocity and angular velocity in the center of mass of linkage i, and m_i is the mass of linkage i. Finally, θ is the angular displacement of the link, and $g = \begin{bmatrix} 0 & -g_0 & 0 \end{bmatrix}^T$ is the gravitational acceleration vector, where $g_0 = 9.81\ m/s^2$.

We combine the model of the motor (Eq. (6)) and the dynamic model of the manipulator (Eq. 7), which can obtain the following model:

$$R_R^2\left[J\ddot{\theta} + \left(B_m + \frac{k_E k_T}{R_a}\right)\dot{\theta}\right] = R_R \frac{k_T}{R_a} u_v - M(\theta)\ddot{\theta} - C\left(\theta, \dot{\theta}\right) - G(\theta) \tag{11}$$

Furthermore, Eq. (11) can be rewritten as follows:

$$D(\theta)\ddot{\theta} + C\left(\theta, \dot{\theta}\right) + B\dot{\theta} + G(\theta) = u_\tau \tag{12}$$

where $D(\theta) = M(\theta) + R_R^2 J$ is the inertia of the link and motor of the robotic arm, $B = R_R^2(B_m + \frac{k_E k_T}{R_a})$ is the friction constant of the robotic arm, and $u_\tau = R_R \frac{k_T}{R_a} u_v$ is the torque of the robotic arm. Finally, we use Eq. (12) in the following controller design.

A. ADAPTIVE SLIIDING MODE CONTROL (ASMC)

We seek to design an advanced controller that can adequately handle the nonlinearity and uncertainty terms and meanwhile gain high robustness and self-tuning properties. Therefore, we combined SMC [21], [22] and an adaptive law [23] for manipulator control (see Fig. 13). The ability to adjust system parameters according to external interference and uncertainty should increase the robustness of the control system in terms of tracking precision.

The control process begins with a comparison of the actual angle and expected angle to obtain the tracking error, which is then input into the SMC to output control voltage to the motor. Introducing the error into the adaptive law allows the

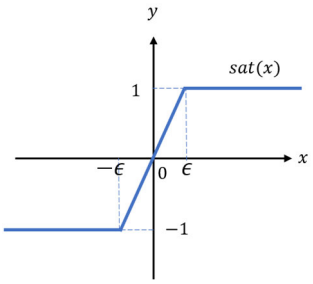

FIGURE 14. Saturation function.

derivation of new adjustment parameters, which are then fed into to the SMC to update its adjustment parameters. After the motor outputs torque to drive the robotic arm, the angle of the arm is fed back to calculate the corresponding error. To compensate for noise interference and differences between the system parameters used to calculate control forces and the actual system parameters, Eq. (12) can be rewritten as follows:

$$D_0(\theta)\ddot{\theta} + C_0\left(\theta, \dot{\theta}\right) + B_0\dot{\theta}_l + G_0(\theta) = u_\tau + d(t) \quad (13)$$

System parameters can be classified into two groups: known items and uncertain items, denoted as $D(\theta) = D_0(\theta) + \Delta D(\theta)$, $C\left(\theta, \dot{\theta}\right) = C_0\left(\theta, \dot{\theta}\right) + \Delta C\left(\theta, \dot{\theta}\right)$, $B = B_0 + \Delta B$, $G(\theta) = G_0(\theta) + \Delta G(\theta)$, where $d(t)$ is the combined effects of control noise and uncertain items. If we define $d_1 = D_0^{-1}(d)$, then the angular acceleration of the robotic arm can be obtained as follows:

$$\ddot{\theta} = -D_0^{-1}\left(C_0 + G_0 + B_0\dot{\theta}\right) + D_0^{-1}(u_\tau) + d_1 \quad (14)$$

Sliding surface s of ASMC is selected as follows:

$$s = \dot{e} + \hat{\lambda}e \quad (15)$$

where $e = \theta_d - \theta$ is the tracking error, which is obtained by subtracting the actual angle θ from the desired angle θ_d, while $\hat{\lambda} > 0$ is the estimated positive adjustment parameter. The careful selection of sliding surface variable s stabilizes the system to attain convergence when the system state is on the sliding surface. Differentiating the sliding surface Eq. (15), we obtain the following:

$$\begin{aligned} \dot{s} &= \ddot{e} + \hat{\lambda}\dot{e} = -\ddot{\theta} + \hat{\lambda}\dot{e} \\ &= D_0^{-1}\left(C_0 + G_0 + B_0\dot{\theta}\right) - D_0^{-1}(u_\tau) - d_1 + \hat{\lambda}\dot{e} \end{aligned} \quad (16)$$

Assume that $\dot{s} = -\hat{\kappa}s - \hat{\eta}sign(s)$, where $\hat{\kappa} > 0$ and $\hat{\eta} > |d_1| > 0$ are the estimated positive adjustment parameters. As shown in Fig. 14, $sign(s)$ is a discontinuous function, which means that it should be replaced with saturation function $sat(s)$, as follows:

$$sat(s) = \begin{cases} 1, & s > \epsilon \\ \dfrac{s}{|\epsilon|}, & -\epsilon \le s \le \epsilon \\ -1, & s < -\epsilon \end{cases} \quad (17)$$

The control signal of the robotic arm can be derived in accordance with Eq. (16) as follows:

$$u_\tau = D_0\left(\hat{\kappa}s + \hat{\eta}sat(s) + \hat{\lambda}\dot{e}\right) + C_0 + G_0 + B_0\dot{\theta} \quad (18)$$

Finally, we can use the updated law to speed up the convergence of error as follows:

$$\dot{\hat{\kappa}} = \sigma_1(s^2 - \gamma_1\hat{\kappa}) \quad (19)$$

$$\dot{\hat{\eta}} = \begin{cases} \sigma_2\left(|s| - \gamma_2\hat{\eta}\right), & |s| \ge \epsilon \\ \sigma_2\left(\dfrac{s^2}{\epsilon} - \gamma_2\hat{\eta}\right), & |s| < \epsilon \end{cases} \quad (20)$$

$$\dot{\hat{\lambda}} = \sigma_3(\gamma_3\hat{\lambda}) \quad (21)$$

where $\sigma_1, \sigma_2, \sigma_3, \gamma_1, \gamma_2, \gamma_3$ are positive constants.

B. STABILITY ANALYSIS

Lyapunov function [24] is widely applied to verify the stability of dynamical systems and control theory. In the current study, we define a positive definite Lyapunov function candidate as follows:

$$V_{ASMC} = \frac{1}{2}s^2 + \frac{1}{2}\frac{1}{\sigma_1}\tilde{\kappa}^2 + \frac{1}{2}\frac{1}{\sigma_2}\tilde{\eta}^2 + \frac{1}{2}\frac{1}{\sigma_3}\tilde{\lambda}^2 \quad (22)$$

where $\tilde{\kappa}$, $\tilde{\eta}$, and $\tilde{\lambda}$ are the estimation errors of κ, η, and λ, respectively defined as $\tilde{\kappa} = \kappa - \hat{\kappa}$, $\tilde{\eta} = \eta - \hat{\eta}$, and $\tilde{\lambda} = \lambda - \hat{\lambda}$. Stability can be analyzed by differentiating Eq. (22) as follows:

$$\begin{aligned} &\dot{V}_{ASMC} \\ &= s\dot{s} + \frac{1}{\sigma_1}\tilde{\kappa}\dot{\tilde{\kappa}} + \frac{1}{\sigma_2}\tilde{\eta}\dot{\tilde{\eta}} + \frac{1}{\sigma_3}\tilde{\lambda}\dot{\tilde{\lambda}} \\ &= s\left(D_0^{-1}\left(C_0 + G_0 + B_0\dot{\theta}\right) - D_0^{-1}(u_\tau) - d_1 + \hat{\lambda}\dot{e}\right) \\ &\quad + \frac{1}{\sigma_1}\tilde{\kappa}\dot{\tilde{\kappa}} + \frac{1}{\sigma_2}\tilde{\eta}\dot{\tilde{\eta}} + \frac{1}{\sigma_3}\tilde{\lambda}\dot{\tilde{\lambda}} \\ &= s\left(D_0^{-1}\left(C_0 + G_0 + B_0\dot{\theta}\right) - D_0^{-1}\left(D_0\left(\hat{\kappa}s + \hat{\eta}sat(s) + \hat{\lambda}\dot{e}\right)\right.\right. \\ &\quad \left.\left. + C_0 + G_0 + B_0\dot{\theta}\right) - d_1 + \hat{\lambda}\dot{e}\right) + \frac{1}{\sigma_1}\tilde{\kappa}\dot{\tilde{\kappa}} + \frac{1}{\sigma_2}\tilde{\eta}\dot{\tilde{\eta}} + \frac{1}{\sigma_3}\tilde{\lambda}\dot{\tilde{\lambda}} \\ &= s\left(-\hat{\kappa}s - \hat{\eta}sat(s) - d_1\right) + \frac{1}{\sigma_1}\tilde{\kappa}\dot{\tilde{\kappa}} + \frac{1}{\sigma_2}\tilde{\eta}\dot{\tilde{\eta}} + \frac{1}{\sigma_3}\tilde{\lambda}\dot{\tilde{\lambda}} \\ &= -\hat{\kappa}s^2 - s\hat{\eta}sat(s) - sd_1 + \frac{1}{\sigma_1}\tilde{\kappa}\dot{\tilde{\kappa}} + \frac{1}{\sigma_2}\tilde{\eta}\dot{\tilde{\eta}} + \frac{1}{\sigma_3}\tilde{\lambda}\dot{\tilde{\lambda}} \end{aligned} \quad (23)$$

In accordance with s selection, this problem can be divided into two cases. In Case 1, if $|s| \ge \epsilon$, then the differentiation of the Lyapunov function candidate can be expressed as follows:

$$\begin{aligned} \dot{V}_{ASMC} &= -\hat{\kappa}s^2 - \hat{\eta}|s| - sd_1 + \frac{1}{\sigma_1}\tilde{\kappa}\dot{\tilde{\kappa}} + \frac{1}{\sigma_2}\tilde{\eta}\dot{\tilde{\eta}} + \frac{1}{\sigma_3}\tilde{\lambda}\dot{\tilde{\lambda}} \\ &= (\tilde{\kappa} - \kappa)s^2 + (\tilde{\eta} - \eta)|s| - s^T d_1 + \frac{1}{\sigma_1}\tilde{\kappa}\dot{\tilde{\kappa}} + \frac{1}{\sigma_2}\tilde{\eta}\dot{\tilde{\eta}} \\ &\quad + \frac{1}{\sigma_3}\tilde{\lambda}\dot{\tilde{\lambda}} \\ &= \tilde{\kappa}\left(s^2 + \frac{1}{\sigma_1}\dot{\tilde{\kappa}}\right) + \tilde{\eta}\left(|s| + \frac{1}{\sigma_2}\dot{\tilde{\eta}}\right) + \tilde{\lambda}\left(\frac{1}{\sigma_3}\dot{\tilde{\lambda}}\right) \\ &\quad - \kappa s^2 - \eta|s| - sd_1 \end{aligned} \quad (24)$$

TABLE 2. Motor parameters.

Parameters	Descriptions	Motor I	Motor II
k_T (Nm/A)	Torque constant	0.0413	0.03867
R_a (Ω)	Terminal resistance	5	2.98
J (kgm^2)	Rotor inertia	0.000026	0.000017
k_E (Vs/rad)	Back-EMF constant	0.04135	0.03867
L_a (H)	Rotor inductance	0.00054	0.000365
B_m (Nms/rad)	Viscous friction constant	0.000009	0.000003
R_R	Reduction ratio	246:1	134:1
Resolution (deg)	Minimum rotation angle	0.001429	0.002624

TABLE 3. Robotic arm parameters.

Parameters	Descriptions	Values
g_0 (m/s^2)	Gravitational acceleration	9.81
m_1 (kg)	Mass of linkage I	0.31
m_2 (kg)	Mass of linkage II	0.24
l_1 (m)	Length of linkage I	0.13
l_2 (m)	Length of linkage II	0.13
l_{c1} (m)	Centroid position length of linkage I	0.065
l_{c2} (m)	Centroid position length of linkage II	0.065

Substituting Eq. (24) into Eq. (19), Eq. (20), and Eq. (21), we obtain the following:

$$\dot{V}_{ASMC} = \gamma_1\tilde{\kappa}\hat{\kappa} + \gamma_2\tilde{\eta}\hat{\eta} + \gamma_3\tilde{\lambda}\hat{\lambda} - \kappa s^2 - \eta\,|s| - sd_1 \quad (25)$$

Due to the fact that

$$\gamma_1\tilde{\kappa}\hat{\kappa} = \gamma_1\tilde{\kappa}\,(\kappa - \tilde{\kappa}) = -\gamma_1\tilde{\kappa}^2 + \gamma_1\tilde{\kappa}\kappa \le -\frac{\gamma_1}{2}\left[|\tilde{\kappa}|^2 - |\kappa|^2\right] \quad (26)$$

$$\gamma_2\tilde{\eta}\hat{\eta} = \gamma_2\tilde{\eta}\,(\eta - \tilde{\eta}) = -\gamma_2\tilde{\eta}^2 + \gamma_2\tilde{\eta}\kappa \le -\frac{\gamma_2}{2}\left[|\tilde{\eta}|^2 - |\eta|^2\right] \quad (27)$$

$$\gamma_3\tilde{\lambda}\hat{\lambda} = \gamma_3\tilde{\lambda}\left(\lambda - \tilde{\lambda}\right) = -\gamma_3\tilde{\lambda}^2 + \gamma_3\tilde{\lambda}\lambda \le -\frac{\gamma_3}{2}\left[\left|\tilde{\lambda}\right|^2 - |\lambda|^2\right] \quad (28)$$

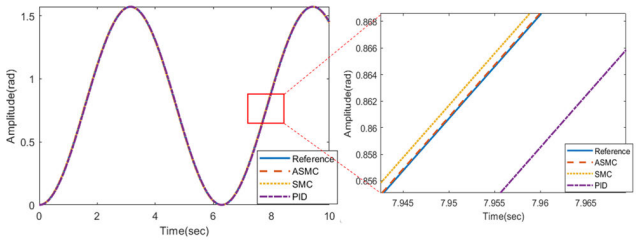

FIGURE 15. (a) Position tracking of Joint-I; (b) Partial enlargement of (a).

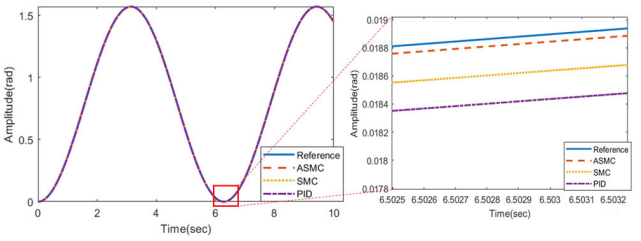

FIGURE 16. (a) Position tracking of Joint-II; (b) Partial enlargement of (a).

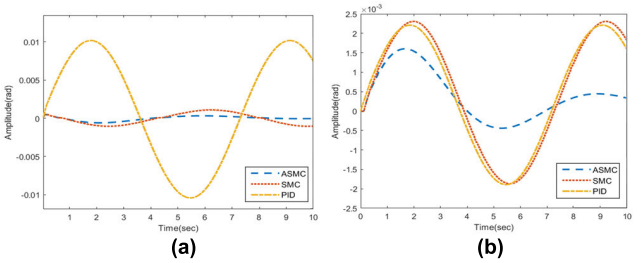

FIGURE 17. (a) Tracking error of Joint-I. (b) Tracking error of Joint-II.

Eq. (25) can be rewritten as

$$\begin{aligned}\dot{V}_{ASMC} &\le -\frac{\gamma_1}{2}\left[|\tilde{\kappa}|^2 - |\kappa|^2\right] - \frac{\gamma_2}{2}\left[|\tilde{\eta}|^2 - |\eta|^2\right] \\ &\quad - \frac{\gamma_3}{2}\left[\left|\tilde{\lambda}\right|^2 - |\lambda|^2\right] - \kappa s^2 - \eta\,|s| - sd_1 \\ &\le -\kappa s^2 - \frac{\gamma_1}{2}|\tilde{\kappa}|^2 - \frac{\gamma_2}{2}|\tilde{\eta}|^2 - \frac{\gamma_3}{2}\left|\tilde{\lambda}\right|^2 - \eta\,|s| \\ &\quad - sd_1 + \frac{\gamma_1}{2}|\kappa|^2 + \frac{\gamma_2}{2}|\eta|^2 + \frac{\gamma_3}{2}|\lambda|^2 \\ &\le -\rho V + \frac{1}{2}\left[\gamma_1|\kappa|^2 + \gamma_2|\eta|^2 + \gamma_3|\lambda|^2\right] \end{aligned} \quad (29)$$

where $\gamma_1, \gamma_2, \gamma_3 > 0$ and $\eta > |d_1|$, such that we select $0 < \rho < \min\{2\kappa, \gamma_1, \gamma_2, \gamma_3\}$.

If the condition $\dot{V}_{ASMC} \ge \frac{1}{2\rho}\left[\gamma_1|\kappa|^2 + \gamma_2|\eta|^2 + \gamma_3|\lambda|^2\right]$ holds, such that $\dot{V} \le 0$, then stability of the system is confirmed.

In Case 2, if $|s| < \epsilon$, then the differentiation of the Lyapunov function candidate can be expressed as follows:

$$\dot{V}_{ASMC} = -\hat{\kappa}s^2 - \hat{\eta}\frac{s^2}{\epsilon} - sd_1 + \frac{1}{\sigma_1}\tilde{\kappa}\dot{\tilde{\kappa}} + \frac{1}{\sigma_2}\tilde{\eta}\dot{\tilde{\eta}} + \frac{1}{\sigma_3}\tilde{\lambda}\dot{\tilde{\lambda}}$$

TABLE 4. Tracking errors associated with the two joints (RMS).

Controllers	Joint I error (rad)	Joint II error (rad)
PID	0.0071	0.0014
SMC	0.0007	0.0014
ASMC (proposed)	0.0003	0.0006

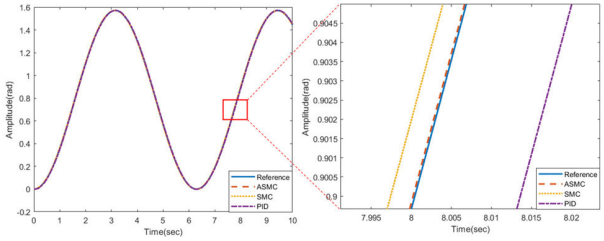

(a) (b)

FIGURE 18. (a) Position tracking of Joint-I with disturbance; (b) Partial enlargement of (a).

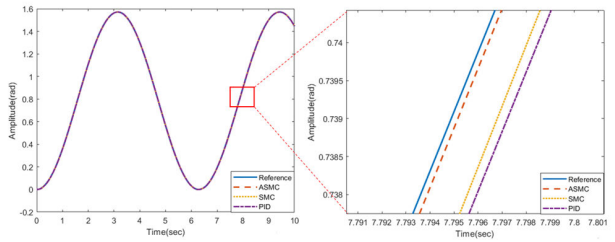

(a) (b)

FIGURE 19. (a) Position tracking of Joint-II with disturbance; (b) Partial enlargement of (a).

$$= (\tilde{\kappa} - \kappa)\, s^2 + (\tilde{\eta} - \eta)\, \frac{s^2}{\epsilon} - s d_1 + \frac{1}{\sigma_1}\tilde{\kappa}\dot{\tilde{\kappa}} + \frac{1}{\sigma_2}\tilde{\eta}\dot{\tilde{\eta}} + \frac{1}{\sigma_3}\tilde{\lambda}\dot{\tilde{\lambda}}$$
$$= \tilde{\kappa}\left(s^2 + \frac{1}{\sigma_1}\dot{\tilde{\kappa}}\right) + \tilde{\eta}\left(\frac{s^2}{\epsilon} + \frac{1}{\sigma_2}\dot{\tilde{\eta}}\right) + \tilde{\lambda}\left(\frac{1}{\sigma_3}\dot{\tilde{\lambda}}\right) - \kappa s^T s - \eta\,|s| - s^T d_1 \tag{30}$$

In accordance with Eq. (19), Eq. (20), and Eq. (21), we can rewrite Eq. (30) as

$$\dot{V}_{ASMC} \le -\frac{\gamma_1}{2}[|\tilde{\kappa}|^2 - |\kappa|^2] - \frac{\gamma_2}{2}[|\tilde{\eta}|^2 - |\eta|^2] - \frac{\gamma_3}{2}[|\tilde{\lambda}|^2 - |\lambda|^2] - \kappa s^2 - \eta\frac{s^2}{\epsilon} - s d_1$$
$$\le -\rho V + \frac{1}{2}[\gamma_1|\kappa|^2 + \gamma_2|\eta|^2 + \gamma_3|\lambda|^2] + \frac{\epsilon|d_1|^2}{4\eta} \tag{31}$$

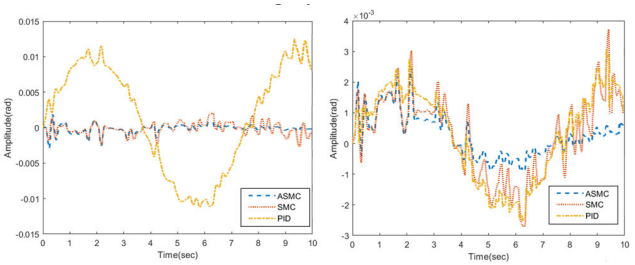

(a) (b)

FIGURE 20. Tracking error of Joint-I with disturbance; (b) Tracking error of Joint-II with disturbance.

TABLE 5. RMS tracking error of Joint-I and Joint-II with disturbance.

Controllers	Joint I error (rad)	Joint II error (rad)
PID	0.0072	0.0015
SMC	0.0015	0.0013
ASMC (proposed)	0.0005	0.0006

where $\gamma_1, \gamma_2, \gamma_3 > 0$ and $\eta > |d_1|$, such that we select $0 < \rho < \min\{2\kappa, \gamma_1, \gamma_2, \gamma_3\}$.

If the condition that $V_{ASMC} \ge \frac{1}{2\rho}\left[\gamma_1 |\kappa|^2 + \gamma_2 |\eta|^2 + \gamma_3 |\lambda|^2\right] + \frac{\epsilon^2 |d_1|^2}{4\eta^2}$ holds, such that $\dot{V} \le 0$, then the stability of the system is confirmed.

Based on stability analysis of Case 1 and Case 2, we can opt for the condition $V_{ASMC} \ge \frac{1}{2\rho}\left[\gamma_1 |\kappa|^2 + \gamma_2 |\eta|^2 + \gamma_3 |\lambda|^2\right] + \frac{\epsilon |d_1|^2}{4\eta}$, which ensures that $\dot{V} \le 0$ in all cases, thereby confirming that the system is stable.

IV. EXPERIMENT

A. SIMULATION SETTINGS

Table 2 lists the parameters of Motor-I and Motor-II based on motor specifications. The parameters of the robotic arm in Table 3 were obtained empirically. The parameters of the three controllers were obtained via trial-and-error as follows: PID ($P_1 = 800$, $I_1 = 1$, $D_1 = 10$, $P_2 = 2000$, $I_2 = 1$, $D_2 = 10$); SMC ($\kappa_1 = 80$, $\eta_1 = 25$, $\lambda_1 = 7000$, $\kappa_2 = 500$, $\eta_2 = 60$, $\lambda_2 = 7000$); Proposed ASMC controller ($\sigma_1 = 0.1$, $\sigma_2 = 0.1$, $\sigma_3 = 0.5$, $\gamma_1 = 0.1$, $\gamma_2 = 0.1$, $\gamma_3 = 0.5$, $\epsilon = 0.002$), and initial κ, η, and λ (the same as SMC). A sine wave was set for the following simulation with a maximum amplitude of 1.57 rad and a period of 6.3 seconds.

B. SIMULATION RESULTS

We first compared the performance of the proposed ASMC controller with that of SMC and PID controllers. A sine wave obtained by tracking the two joints can be used to maintain the angle of the robot arm between 0 and 90 degrees (π /2 rad) for the analysis of tracking performance in terms of tracking

error, as follows:

$$\theta_d = \frac{\pi}{4} sin\left(t + \frac{3\pi}{2}\right) + \frac{\pi}{4} \tag{32}$$

Fig. 15(a) presents the tracking trajectory of Joint-1, where the solid line indicates the reference trajectory, the dashed line indicates the proposed controller, the dotted line indicates the conventional SMC, and the dash dot line indicates the PID controller. We can see in the enlarged image in Fig.15(b) that the largest deviation from the reference was generated by the PID, respectively followed by SMC and ASMC. Fig. 16(a) presents the tracking trajectories of Joint-II using the three controllers. We can see in the enlarged image in Fig.16(b) that the results obtained using ASMC were the closest to the reference trajectory, due presumably to adaptive adjustment.

As shown in Fig. 17(a), ASMC achieved the lowest tracking error for Joint-I. As shown in Fig. 17(b), despite the fact that the tracking error of Joint-II also included the tracking error of Joint-I, the tracking error of ASMC was still close to 0.

We also calculated the Root Mean Square (RMS) tracking error as follows:

$$e_{rms} = \sqrt{\frac{1}{n}\sum_{k=1}^{n} e_{(k)}^2} \tag{33}$$

As shown in Table 4, the PID controller generated the largest tracking error followed by SMC. Note that ASMC and SMC shared the same initial parameter values; however, the inclusion of the learning law in ASMC led to a rapid decrease in tracking error, such that after learning for 10 seconds, the RMS error of ASMC at Joint-I was half that of SMC and 20 times lower than that of PID. The RMS error of ASMC at Joint-II was roughly half that of SMC and PID.

As shown in Eq. (34), the robustness of ASMC was assessed by adding signal disturbance (generated using MATLAB Simulink) to the torque measurements.

$$d = \begin{cases} Noise\ power = 0.1\ Nm \\ Sample\ time = 0.1\ s \\ Seed = 23341 \end{cases} \tag{34}$$

Fig. 18(a) and Fig. 19(a) respectively present the tracking trajectories of Joint-I and Joint-II with added signal disturbance. The corresponding enlargements in Fig. 18(b) and Fig. 19(b) revealed that the results obtained under disturbance conditions were nearly the same as those obtained under ideal conditions. Fig. 20(a) and Fig. 20(b) respectively present the errors in tracking Joint-I and Joint-II with added signal disturbance. The tracking errors oscillated considerably when the signal disturbance was first added; however, ASMC rapidly converged at 0. Eq. (33) was used to quantify the tracking errors with added disturbance, the results of which are shown in Table 5.

C. EXPERIMENT SETUP AND SETTING

Fig. 21 presents a photograph of the experiment used to assess the proposed robotic arm. For Motor-I, we used a DC-micromotor equipped with a 246:1 reducer and 1024 encoder (FAULHABER Series 3242024CR). For Motor-II, we used a similar DC-Micromotor equipped with a 134:1 reducer and 1024 encoder (FAULHABER Series

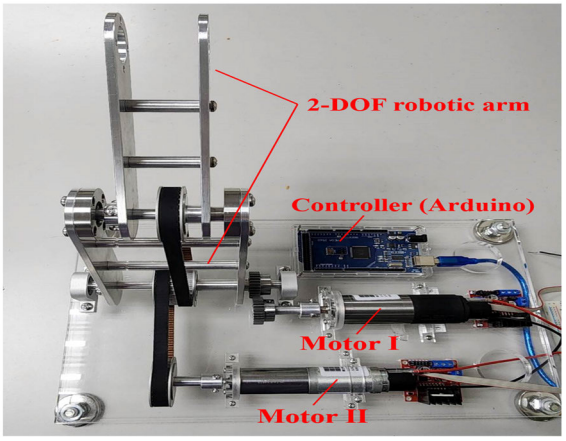

FIGURE 21. Photograph of proposed robotic arm used in experiments.

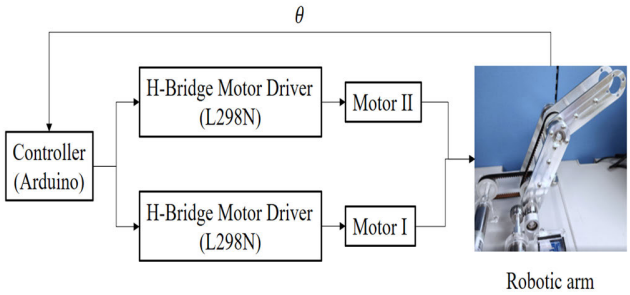

FIGURE 22. Schematic diagram showing the relationships among components in the experiment.

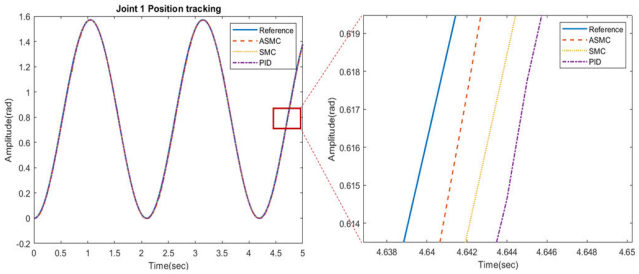

FIGURE 23. (a) Position tracking of Joint-I; (b) Partial enlargement of (a).

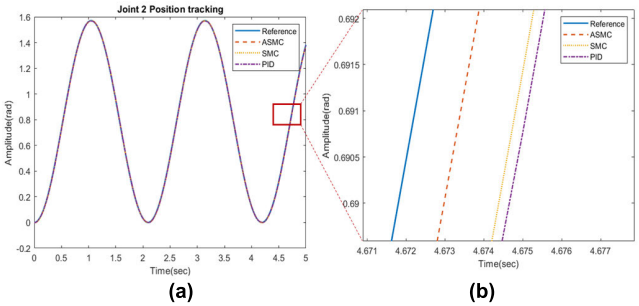

FIGURE 24. (a) Position tracking of Joint-II; (b) Partial enlargement of (a).

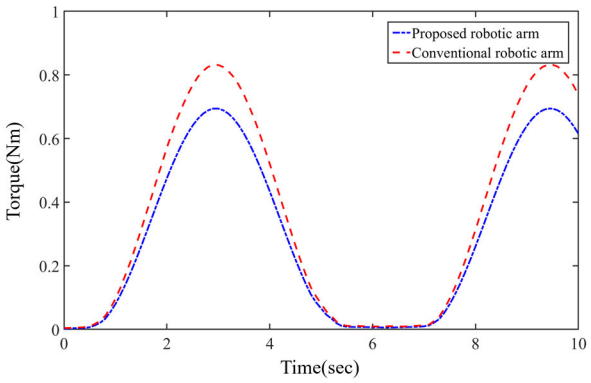

FIGURE 25. Comparison between the torque induced of the conventional and proposed robotic arms.

TABLE 6. RMS tracking errors of the two joints.

Controllers	Joint I error (rad)	Joint II error (rad)
PID	0.0075	0.004
SMC	0.0062	0.0035
ASMC (proposed)	0.0058	0.0022

2657024CR). We selected an H-Bridge motor driver and L298N PWM to control the direction of rotation, as this setup would handle a maximum voltage of 46V and a continuous working current of 2A, which is suitable for the two motors.

As shown in Fig. 22, the experiments in this paper involved uploading the control program written in MATLAB Simulink to the Arduino platform as follows:

1. The controller transmits signals for forward or reverse rotation and PWM signals to the H-Bridge motor driver in accordance with the data it receives.
2. The controller then receives an angle value returned by the encoder on the robotic arm.
3. The controller calculates the tracking error for the subsequent control operation.

The experiment involved tracking a sine wave with an initial angle of 0, a maximum amplitude of 1.57 rad, and a period of 6.3 seconds. Based on trial-and-error, the controller parameters were adjusted as follows: PID ($P_1 = 650, I_1 = 8, D_1 = 16, P_2 = 900, I_2 = 4, D_2 = 12$); SMC ($\kappa_1 = 3, \eta_1 = 1500, \lambda_1 = 200, \kappa_2 = 200, \eta_2 = 6, \lambda_2 = 4000$); Proposed ASMC ($\sigma_1 = 0.1, \sigma_2 = 0.1, \sigma_3 = 0.5, \gamma_1 = 0.01, \gamma_2 = 0.01, \gamma_3 = 0.05, \epsilon = 0.002$). Note that the initial κ, η, and λ of two joints were the same as SMC.

D. EXPERIMENT RESULTS

Fig. 23(a) and Fig. 24(a) present the tracking trajectories of Joint-I and Joint-II, where the solid line indicates the reference trajectory, the dashed line indicates the proposed controller, the dotted line indicates the traditional SMC, and the dash dot line indicates the PID controller. As shown in the enlarged images in Fig. 23(b) and Fig. 24(b), the tracking trajectories of Joint-I and Joint-II were close to those obtained in simulations. Eq. (28) was used to quantify the tracking errors of the robotic arm, the results of which are shown in Table 6. ASMC clearly outperformed the other control methods. Note however that the mechanical components and power transmission system introduced many uncertainties that were absent from the simulations, which resulted in more obvious errors.

In a final experiment, we reconfigured the robotic arm to emulate a conventional design with Motor-II installed at Joint-II, such that the weight of Motor-II (0.16kg) was added to the total torque generated during the rotation of Joint-I. The experiment was set to track the same trajectory, which result is shown in Fig. 25. The maximum torque values of the proposed and conventional manipulators were 0.694 Nm and 0.831 Nm. The proposed one was 16% less than that of the manipulators; thus, the proposed design can effectively reduce the torque induced during the robotic arm movement.

V. CONCLUSION

This paper presents a two-axis robot arm with a novel mechanical design with the motor installed on the base of the devices to reduce the torque induced by arm movements. However, the proposed design used the belts to transmit the motor power to the linkages, which may cause the unwanted slipping phenomenon when the robotic arm carries a heavy load. In the future, we are considering using the chains instead of the belts to ease this potential issue. In modeling and controller, we combined the nominal dynamic models of the manipulator and motor to fully account for the model uncertainties and external disturbances that the manipulator is likely to encounter during operations. We then developed an advanced controller to resolve these issues and thereby ensure the precise tracking of the desired trajectory. The proposed controller uses the sliding mode control method in conjunction with an adaptive law to calculate the voltage requirements and control voltage is delivered through by a PWM input. In simulations and experiments, the proposed controller outperformed other controllers (PID and SMC) in terms of errors generated during trajectory tracking. The proposed controller demonstrated excellent stability and robustness without the need for sliding mode artificial parameter adjustment. We also provide empirical evidence demonstrating the efficacy of the proposed design in reducing the torque generated by robot arm movements.

REFERENCES

[1] Y. He, X. Mai, C. Cui, J. Gao, Z. Yang, K. Zhang, X. Chen, Y. Chen, and H. Tang, "Dynamic modeling, simulation, and experimental verification of a wafer handling SCARA robot with decoupling servo control," *IEEE Access*, vol. 7, pp. 47143–47153, 2019.

[2] D.-H. Lee, M.-S. Choi, H. Park, G.-R. Jang, J.-H. Park, and J.-H. Bae, "Peg-in-hole assembly with dual-arm robot and dexterous robot hands," *IEEE Robot. Autom. Lett.*, vol. 7, no. 4, pp. 8566–8573, Oct. 2022.

[3] J. Roy and L. L. Whitcomb, "Comparative structural analysis of 2-DOF semi-direct-drive linkages for robot arms," *IEEE/ASME Trans. Mechatronics*, vol. 4, no. 1, pp. 82–86, Mar. 1999.
[4] P. Yadmellat, A. S. Shafer, and M. R. Kermani, "Design and development of a single-motor, two-DOF, safe manipulator," *IEEE/ASME Trans. Mechatronics*, vol. 19, no. 4, pp. 1384–1391, Aug. 2014.
[5] H.-S. Kim, J.-K. Min, and J.-B. Song, "Multiple-degree-of-freedom counterbalance robot arm based on slider-crank mechanism and bevel gear units," *IEEE Trans. Robot.*, vol. 32, no. 1, pp. 230–235, Feb. 2016.
[6] J.-K. Min, D.-W. Kim, and J.-B. Song, "A wall-mounted robot arm equipped with a 4-DOF yaw-pitch-yaw-pitch counterbalance mechanism," *IEEE Robot. Autom. Lett.*, vol. 5, no. 3, pp. 3768–3774, Jul. 2020.
[7] Y. Huang, Y. Chen, X. Zhang, H. Zhang, C. Song, and J. Ota, "A novel cable-driven 7-DOF anthropomorphic manipulator," *IEEE/ASME Trans. Mechatronics*, vol. 26, no. 4, pp. 2174–2185, Aug. 2021.
[8] V. Groenhuis, G. Rolff, K. Bosman, L. Abelmann, and S. Stramigioli, "Multi-axis electric stepper motor," *IEEE Robot. Autom. Lett.*, vol. 6, no. 4, pp. 7201–7208, Oct. 2021.
[9] M. H. Korayem, A. Hedayat, and S. F. Dehkordi, "Dynamic modeling of cooperative manipulators with frictional contact at the end effectors," *Appl. Math. Model.*, vol. 90, pp. 302–326, Feb. 2021.
[10] M. Aghajari, S. F. Dehkordi, and M. H. Korayem, "Nonlinear dynamic analysis of the extended telescopic joints manipulator with flexible links," *Arabian J. Sci. Eng.*, vol. 46, no. 8, pp. 7909–7928, Aug. 2021.
[11] J. Baek, S. Cho, and S. Han, "Practical time-delay control with adaptive gains for trajectory tracking of robot manipulators," *IEEE Trans. Ind. Electron.*, vol. 65, no. 7, pp. 5682–5692, Jul. 2018.
[12] Q. Guo, Y. Zhang, B. G. Celler, and S. W. Su, "Neural adaptive backstepping control of a robotic manipulator with prescribed performance constraint," *IEEE Trans. Neural Netw. Learn. Syst.*, vol. 30, no. 12, pp. 3572–3583, Dec. 2019.
[13] Y. Zhu, J. Qiao, Y. Zhang, and L. Guo, "High-precision trajectory tracking control for space manipulator with neutral uncertainty and deadzone nonlinearity," *IEEE Trans. Control Syst. Technol.*, vol. 27, no. 5, pp. 2254–2262, Sep. 2019.
[14] J. Nubert, J. Köhler, V. Berenz, F. Allgöwer, and S. Trimpe, "Safe and fast tracking on a robot manipulator: Robust MPC and neural network control," *IEEE Robot. Autom. Lett.*, vol. 5, no. 2, pp. 3050–3057, Apr. 2020.
[15] B. Xiao, L. Cao, S. Xu, and L. Liu, "Robust tracking control of robot manipulators with actuator faults and joint velocity measurement uncertainty," *IEEE/ASME Trans. Mechatronics*, vol. 25, no. 3, pp. 1354–1365, Jun. 2020.
[16] J. Lee, P. H. Chang, and M. Jin, "An adaptive gain dynamics for time delay control improves accuracy and robustness to significant payload changes for robots," *IEEE Trans. Ind. Electron.*, vol. 67, no. 4, pp. 3076–3085, Apr. 2020.
[17] Y. Lin, Z. Chen, and B. Yao, "Unified motion/force/impedance control for manipulators in unknown contact environments based on robust model-reaching approach," *IEEE/ASME Trans. Mechatronics*, vol. 26, no. 4, pp. 1905–1913, Aug. 2021.
[18] N. Mohan, T. M. Undeland, and W. P. Robbins, *Power Electronics: Converters Applications and Design*, 3rd ed. New Delhi, India: Wiley, 2007.
[19] M. W. Spong, S. Hutchinson, and M. Vidyasagar, *Robot Dynamics and Control*, 2nd ed. Hoboken, NJ, USA: Wiley, 2004.
[20] J. Angeles, *Fundamentals of Robotic Mechanical Systems: Theory, Methods, and Algorithms*, 3rd ed. Berlin, Germany: Springer, 2007.
[21] B. Ren, Y. Wang, and J. Chen, "A novel robust finite-time trajectory control with the high-order sliding mode for human–robot cooperation," *IEEE Access*, vol. 7, pp. 130874–130882, 2019.
[22] D. Nicolis, F. Allevi, and P. Rocco, "Operational space model predictive sliding mode control for redundant manipulators," *IEEE Trans. Robot.*, vol. 36, no. 4, pp. 1348–1355, Aug. 2020.
[23] P. A. Ioannou and J. Sun, *Robust Adaptive Control*. Englewood Cliffs, NJ, USA: Prentice-Hall, 1996.
[24] H. K. Hassan, *Nonlinear Systems*, 3rd ed. Upper Saddle River, NJ, USA: Prentice-Hall, 2001.

JIM-WEI WU (Member, IEEE) received the B.S. and M.S. degrees from National Taiwan Normal University, Taipei, Taiwan, in 2005 and 2007, respectively, and the Ph.D. degree in electrical engineering from National Taiwan University, Taipei, in 2013. He is currently a member and an Assistant Professor with the Department of Electrical Engineering, National Central University, Taoyuan City, Taiwan. His research interests include robotic systems, visual technology, precision positioning control, micro-/nano-measurement systems, and advanced control theory and applications.

TZU-LIN LEE was born in New Taipei City, Taiwan, in 1999. She received the B.S. degree in electrical engineering from National United University, Taiwan, in 2021, and the M.S. degree in electrical engineering from National Central University, Taoyuan City, Taiwan, in 2023. Her research interests include robotic arm systems, and advanced control theory and applications.

YOU-CHENG YAN received the B.S. degree in intelligent machinery from National Central University, Taoyuan City, Taiwan, in 2022, where he is currently pursuing the M.S. degree in electrical engineering. His research interests include robotic arm systems, adaptive control theory, optimal control theory, and relative applications.

CHUAN-AN CHOU was born in New Taipei City, Taiwan, in 1999. She received the B.S. degree in electrical engineering from Fu Jen Catholic University, Taipei, Taiwan, in 2022. She is currently pursuing the M.S. degree in electrical engineering with National Central University, Taoyuan City, Taiwan. Her research interests include robotic arm systems, and advanced control theory and applications.

CHENG-CHANG HO was born in Taipei, Taiwan, in 1981. He received the Ph.D. degree in electrical engineering from National Taiwan University, in 2014. He is currently an Assistant Professor with the Department of Electronic Engineering, Lunghwa University of Science and Technology, Taoyuan City, Taiwan. His research interests include robot controls, technologies of dual quaternion, and pattern recognition.